Biofabrication

PAPER

Net shape fabrication of calcium phosphate scaffolds with multiple material domains

Yangmin Xie[1], Laurence E Rustom[2], Anna M McDermott[3], Joel D Boerckel[3], Amy J Wagoner Johnson[4], Andrew G Alleyne[4] and David J Hoelzle[3,5]

[1] Shanghai Key Laboratory of Intelligent Manufacturing and Robotics, School of Mechatronics Engineering and Automation, Shanghai University, Shanghai, People's Republic of China, 200444
[2] Dept. of Bioengineering, University of Illinois at Urbana-Champaign, Urbana, IL 61801, USA
[3] Dept. of Aerospace and Mechanical Engineering, University of Notre Dame, Notre Dame, IN 46556, USA
[4] Dept. of Mechanical Science and Engineering, University of Illinois at Urbana-Champaign, Urbana, IL 61801, USA
[5] Author to whom any correspondence should be addressed.

E-mail: dhoelzle@nd.edu

Keywords: tissue engineering, additive manufacturing, calcium phosphate materials, patient specific grafts

RECEIVED
5 June 2015

REVISED
14 September 2015

ACCEPTED FOR PUBLICATION
27 October 2015

PUBLISHED
8 January 2016

Abstract

Calcium phosphate (CaP) materials have been proven to be efficacious as bone scaffold materials, but are difficult to fabricate into complex architectures because of the high processing temperatures required. In contrast, polymeric materials are easily formed into scaffolds with near-net-shape forms of patient-specific defects and with domains of different materials; however, they have reduced load-bearing capacity compared to CaPs. To preserve the merits of CaP scaffolds and enable advanced scaffold manufacturing, this manuscript describes an additive manufacturing process that is coupled with a mold support for overhanging features; we demonstrate that this process enables the fabrication of CaP scaffolds that have both complex, near-net-shape contours and distinct domains with different microstructures. First, we use a set of canonical structures to study the manufacture of complex contours and distinct regions of different material domains within a mold. We then apply these capabilities to the fabrication of a scaffold that is designed for a 5 cm orbital socket defect. This scaffold has complex external contours, interconnected porosity on the order of 300 μm throughout, and two distinct domains of different material microstructures.

1. Introduction

Bone defects that are above a critical size will not spontaneously heal when treated by mechanical fixation alone [1–3]. This critical size is a function of defect location and the integrity of surrounding tissue. Skeletal defects of this severity can compromise patient ambulatory, masticatory, or dexterity function and thus lead to a considerable decrease in patient quality of life. Loss or injury of skeletal mass can be the result of myriad factors, including acute trauma leading to fragmented or segmental defects [4], resorption from chronic diseases such as tooth decay [5], or surgical removal after oncological radiation treatments for bone or adjacent tissue neoplasia [3]. The current 'gold standard' for large bone defect repair is the autograft, a procedure in which healthy bone tissue is harvested from a donor site on the patient, typically the iliac crest or floating ribs, sculpted into the approximate shape of the defect void, and then fixed in place with metal or polymer hardware [6]. In defect regions with a rich blood supply, and hence supply of osteoprogenitor cells, graft bone is simply fixtured and then packed with morcelized autograft remnants or bone paste. Long bone defects often have a poor blood supply and a two-stage Masquelet technique is commonly used to prime the defect location for autograft integration [7, 8]; alternate strategies for segmental bone defects in long bones do not utilize autologous bone [9]. An autologous bone graft has excellent osteoinductive and osteoconductive capabilities; however, the harvest requires an additional surgery, leading to donor site morbidity [10], and there is an inadequate supply of autologous bone for complex cases [3].

Tissue engineering has promise for solving the harvest surgery morbidity and inadequate supply

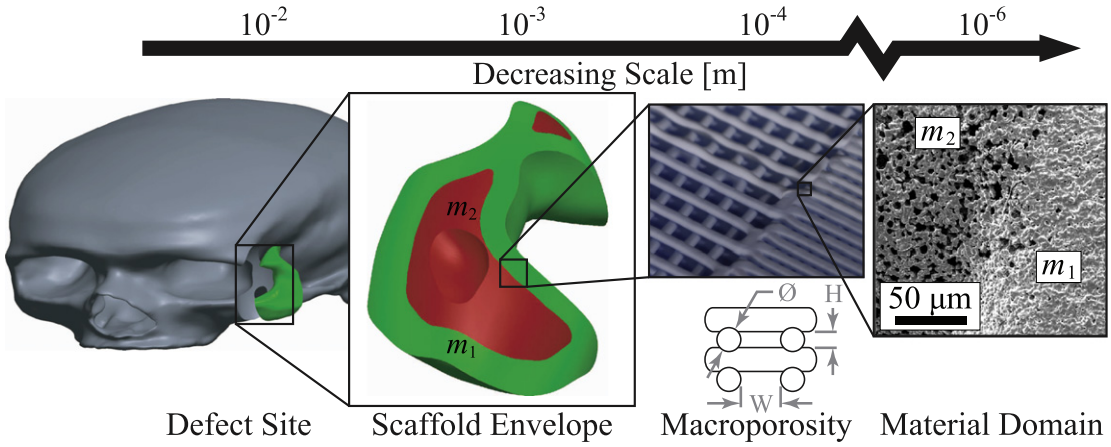

Figure 1. Scaffold design space. In this example, the defect site is a 5 cm-long portion of the orbital socket. The scaffold envelope is the digital negative of the missing bone tissue. Both the macroporosity (filament spacing) and material domain can be designed such that different domains have different moduli, pore connectivities, surface areas, or material types. The photographs of macroporosity and material domain are used with permission from the American Society of Mechanical Engineers.

limitations of autografts. Although researchers have demonstrated clinical success with engineered soft, tubular or planar tissues [11, 12], clinical translation has been slow for complex, three-dimensional (3D), and load-bearing tissues such as bone [13]. For the replacement of large (greater than 3 cm) areas of damaged bone, tissue-engineered constructs have not demonstrated the osteoinductive, osteoconductive, and load-bearing capabilities of autografts [13].

Tissue-engineered constructs for bone typically consist of: a scaffold, to provide a 3D template for natural bone remodeling; biologics such as antibiotics, growth factors, or cells; and fixation hardware to secure the construct in place [6, 14]. This manuscript focuses on the manufacture of advanced architecture scaffolds made from calcium phosphate (CaP) materials. We define advanced architecture scaffolds as scaffolds that can be designed and manufactured on three hierarchical levels (figure 1): the envelope that defines the 3D space occupied by the scaffold; macroscale porosity (pore interconnections on the order of 150–1000 μm) that permits osteoprogenitor cell migration and blood vessel development [15, 16]; and the material domain, which defines the chemical and microstructural properties in each spatial domain of the scaffold. Scaffolds of this complexity can only be manufactured by additive manufacturing (AM) tools, more commonly called 3D printers.

We are interested in advanced architecture scaffold manufacturing by AM with the CaP materials class, a well-studied bioceramic for bone tissue engineering. However, CaP scaffolds with the advanced architectural features shown in figure 1 are considerably more difficult to manufacture than their polymeric counterparts. In comparison to purely CaP scaffolds, polymeric scaffolds and CaP/polymer composite scaffolds with a high concentration (>15%) of polymeric binders can be formed into advanced architectures by commercial AM tools that utilize one of the many material-consolidation mechanisms available for polymer materials. Some of the earliest studies of advanced architecture scaffolds used a phase transition either by local heating (to about 100 °C) and then cooling, or by freeze-forming, to consolidate filamentous or powdered polymeric feedstock [17–24]. The adhesive nature of polymeric binders has been utilized in binder jet printing AM tools to create purely polymeric scaffolds and CaP/polymeric composites [25–28]. Importantly, CaP/polymeric composites have a ductile failure mechanism [28], unlike the brittle failure mechanism of pure CaP materials. However, CaP particles are held together by the polymer network and thus the ultimate stress of a CaP/polymeric composite is lower than that of pure CaP, and below the threshold required for load-bearing applications [28, 29]. Currently, an active research thrust is the study of natural hydrogels, cross-linked by a chemical or photochemical mechanism, to construct non-load-bearing scaffolds [30–35]. Hydrogel materials have a highly modifiable chemical structure that has permitted researchers to attach and sequester growth factors and drugs for spatiotemporal control of release [36–39]. Natural collagen and CaP/collagen composites, consolidated by freeze forming [22, 40], have demonstrated higher moduli than hydrogels, but the moduli are still an order of magnitude below load-bearing requirements [22, 41].

Although polymers enable complex architecture scaffolds, there are distinct advantages to working with purely CaP materials for load-bearing scaffolds. The degradation products of a CaP scaffold are thought to create a supersaturation of calcium and phosphate ions that are then directly used in bone formation and remodeling [42]. In contrast, the degradation products of many polymeric materials are toxic or can cause an inflammatory response [43]. However, a

notable disadvantage of CaP materials is that they are brittle, causing concern for applications requiring significant load-bearing capacity [29, 44]. *In vivo* studies demonstrate that new bone growth reinforces the brittle ceramic network to increase material toughness [44]. In contrast to the moderate temperatures (on the order of 100 °C) used with polymer scaffolds, extremely high temperatures (>1000 °C) are required to sinter green bodies. This requirement has limited CaP manufacturing to bulk processing methods (regular envelopes, random macroporosity, and a single material) and AM-based manufacturing where researchers have demonstrated simple envelopes, advanced macroporosity designs, and often a single material throughout. The authors [45] and others [46, 47] have previously demonstrated scaffolds with a simple cylindrical envelope and with multiple macroporosities.

This work demonstrates new manufacturing capabilities for CaP materials. The unique aspect of this work is the combined ability to fabricate near-net-shape, complex scaffold envelopes and to integrate multiple CaP building materials into a single scaffold (figure 1). We define a region that contains a unique building material as a material domain. The incorporation of multiple material domains could mean the incorporation of CaPs of different chemical composition, such as hydroxyapatite (HA) and tricalcium phosphate (TCP). Multiple material domains could also mean that the final scaffold consists of multiple domains with the same chemical composition, but different microporosity. In the latter case, sacrificial porogens can be incorporated into the building material and, after sintering, the domains will have a porous microstructure from porogen removal.

The design space is motivated by the needs of the bone tissue engineering community. However, as this is a manufacturing study, the tested designs are not explicitly tailored to elicit a particular *in vivo* response. AM tools enable the fabrication of a structure containing interconnected macroporosity that will provide a conduit for osteoprogenitor cell migration and blood vessel formation distant from the native tissue. Previous *in vivo* results demonstrate that a pore interconnection size of 100–1000 μm is appropriate for bone formation [42, 43]. The scaffold material domain, defined in the previous paragraph, is an important design consideration that influences scaffold biocompatibility, mechanical properties, surface topography, and *in vivo* response. Here we study scaffolds with multiple spatial domains of distinct materials; we study a high density HA material (m_1 in figure 1) and a HA material with a 50% nominal microscale porosity after sintering (m_2 in figure 1, pore size of 4.86 $\pm$ 3.62 μm [48]). Microscale porosity within a CaP scaffold has been shown to provide a roughened surface for cellular filopodia attachment [49, 50] and enhanced angiogenesis at early time points for improved initial deposition of woven bone [16]. Furthermore, a higher local concentration of the proteins and ions required for bone formation, and possibly even osteogenic growth factors, is thought to be present in micropores *in vivo*, as compared to non-microporous HA [43, 51, 52]. In particular, our group has demonstrated that HA scaffolds with an interconnected network of microscale porosity yield a more uniform growth profile for new bone than scaffolds without microscale porosity [53, 54]; the hypothesized mechanism is that capillary forces from the microporous network draw endogenous osteoprogenitor cells deep within the scaffold, priming the scaffold for new bone growth distant from the native bone tissue [55]. However, materials with microscale pores are mechanically weaker, and thus there may be clinical advantages to interlaying a stronger, denser material with a high porosity material.

Finally, we advocate that near-net-shape fabrication is required to efficiently use patient-specific 3D imaging data to define the scaffold envelope. To accomplish this, it is critical that overhanging and unsupported features can be reliably fabricated without post-fabrication subtractive manufacturing processes, such as machining or grinding, to shape the scaffold to match a particular defect [5, 44, 53, 54]; this is a time-consuming step and risks scaffold damage, particularly for ceramics. Polymer-based AM processes such as fused deposition modeling commonly integrate sacrificial material regions into the building routine to support the large overhanging features [56]. The sacrificial material is subsequently removed by dissolving it in water or by fracture at an intentionally weak interface. CaP green bodies are water-soluble and susceptible to cracking before sintering; therefore sacrificial materials that dissolve or delaminate are not a viable solution. Another sacrificial material option is a polymer that is melted away during sintering [57]; however, to maintain fabrication accuracy the fluid viscosities of the building materials must be carefully matched so that a ceramic deposited onto a polymer does not deform the polymer and vice versa. Given the vastly different material characteristics of polymeric and ceramic particles, and therefore different colloidal synthesis methods, matching these rheological properties is a difficult task. This work presents an alternative approach to build large unsupported features. In this two-step method, we build the net shaped part within a polymer mold manufactured by stereolithography. The molds fabricated by stereolithography are inexpensive and can be manufactured in just hours. Critically, the method permits many of the conceivable features for a bone scaffold to be fabricated. The set of feasible features will be discussed in more detail in section 4.

This work investigates two main capabilities: (1) the manufacture of complex scaffold envelopes by utilizing both the self-supporting nature of layer-by-layer AM fabrication for steep draft angles and the use of molds for shallow draft angles, and (2) the integration

of different material domains within a single scaffold. To fully explore these manufacturing capabilities, we fabricated and characterized several scaffold designs. First, we used basic scaffold shapes to evaluate the fabrication of a scaffold on a mold surface. These fundamental experiments determined the range of overhanging features that could be readily fabricated. Second, we utilized three different canonical scaffolds to evaluate the navigation of the AM system within more complex molds and the integration of multiple material domains within a single scaffold. Finally, using the knowledge gained from these initial studies, we manufactured a large anatomically derived scaffold comprising complex unsupported contours, interconnected macroporosity, and domains of different material microstructures. The use of an anatomical design demonstrates a clinically applicable process plan that steps through 3D imaging, fabrication planning, and fabrication, and thus provides a blueprint for patient-specific CaP scaffold manufacture.

2. Materials and methods

2.1. Materials

The manufacturing system utilizes colloidal build materials with a carefully tuned rheology such that the material extrudes through small (inner diameter $d = O(500\ \mu\text{m})$) nozzles, yet holds its shape such that 3D structures can be fabricated in a layer-by-layer process. Characteristically, these are yield-pseudoplastic fluids, which are described by the Herschel-Bulkley model, equation (1). Yield-pseudoplastic fluids maintain their shape under low shear-stress conditions where the shear-stress, τ, is below the yield stress, τ_y, and then the viscosity decreases as it is sheared, such as during extrusion through a nozzle [58, 59].

$$\begin{aligned} \tau &= \tau_y + m\dot{\gamma}^n \quad \text{for } |\tau| > \tau_y \\ \dot{\gamma} &= 0 \qquad \text{for } |\tau| \leqslant \tau_y \end{aligned} \tag{1}$$

The shear-rate is given by $\dot{\gamma}$, the fluid consistency index by m, and the flow behavior index by n; a fluid is shear-thinning when $0 < n < 1$. Here we demonstrate two different build material formulations, one in which the solid phase of the colloid is purely HA particles (median particle diameter of $1.75 \pm 1.04\ \mu$m, Reidel de-Haen, Sigma Aldrich 04238), m_1, and the other in which the solid phase is 50 vol% HA particles and 50 vol% poly(methyl methacrylate) (PMMA) microbeads ($5.96 \pm 2.00\ \mu$m [48], M-100, Sekisui Plastics Co., Ltd., Japan), m_2. The colloid formulation is described by Michna *et al* in [60] and in a detailed protocol provided in [61]; for filaments of the size used here, material rheology is adjusted by pH modification until the rheological measurements are $\tau_y = O(40\ \text{Pa})$, $m = O(60\ \text{Pa sec}^n)$, and $n = O(0.40)$ [62, 63]. A complete introduction to the science of colloidal processing can be found in [59], and appropriate rheological parameters τ_y, m, and n for different applications can be found in the references in Lewis's comprehensive review article [57]. Material m_1 has a 45/55 vol% solid-to-liquid phase ratio, and material m_2 has a 55/45 solid-to-liquid phase ratio. After post-process sintering, described in section 2.3, material m_2 is devoid of polymer; however, an interconnected microporous network is formed by the volatilization of the PMMA microbeads, yielding a porosity of approximately 50 vol% and pore size of $4.86 \pm 3.62\ \mu$m [48]. Representative images of the microstructures of m_1 and m_2 are shown in figure 1. A complete materials characterization of the HA powder and colloids used here is outside the scope of this manufacturing study; the interested reader can find these results in references [44, 48, 53, 54, 63, 64].

Molds are fabricated by a standard stereolithography AM system (ProtoGen O-XT 18420 Resin, Viper SI SLA, 3D Systems, Rock Hill, SC) with a resolution of 0.05 mm in the x and y axes and 0.025 mm in the z axis. Mold manufacture is more accurate than the manufacture of CaP scaffolds, hence mold fabrication is not an accuracy-limiting process step and is not discussed further here.

2.2. Digital manipulation of scaffold designs and machine language

All AM processes are instructed by a base digital 3D model of the desired structure that is in one of the many 3D model file formats (PTC Creo .prt files were used in these examples). This model is converted to a triangulated surface rendering as a .stl file. Each .stl file is converted to G-Code, a standard manufacturing instruction language [65]. Here, we use the open-source converter Skeinforge (RepRap.org). G-Code instructions for direct-write AM tools are simple compared to a CNC mill; the two basic commands are the linear move in which the next way-point in space (X, Y, Z) is specified, and micro-extruder commands in which an individual micro-extruder is commanded to start or stop extrusion.

2.3. Manufacturing system and process

The scaffolds are fabricated using a custom-built direct-write AM system called micro-Robotic Deposition (μRD) [66, 67]. μRD fabricates complex 3D structures by coordinating the extrusion of the colloidal building material with the positioning of the extruder nozzle in 3D space (figure 2). Nozzle position is driven by a large travel (>1 m travel in the x and y directions and >100 mm in the z direction) gantry system (Aerotech AGS 10 000), and extrusion is controlled by an array of servo-controlled micro-extruders that drive the colloidal building material through a nozzle to generate extruded filaments that

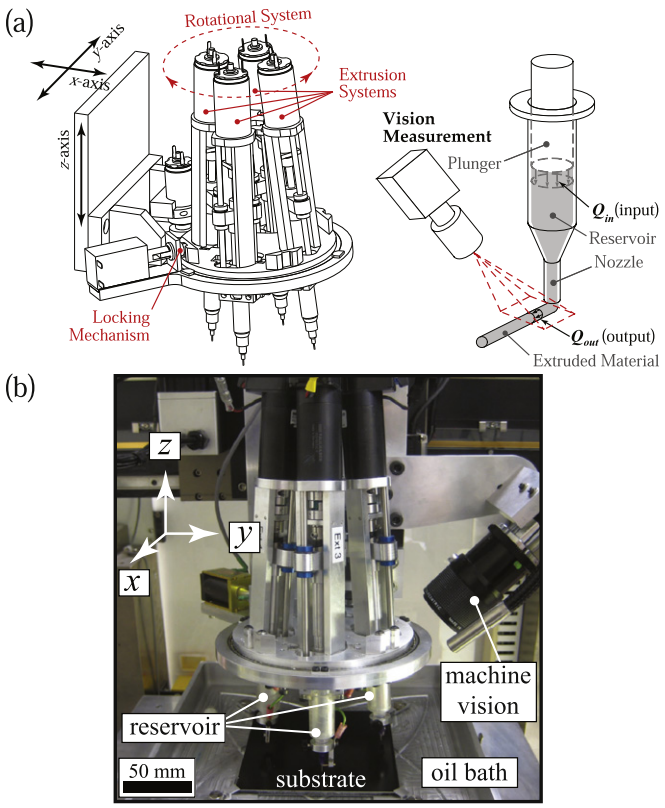

Figure 2. Micro-Robotic Deposition (μRD) manufacturing system. (a) Engineering schematic of a multi-material extrusion head and an individual extrusion system. Material extrusion, Q_{out}, is driven by the servo-controlled displacement of a plunger, Q_{in}, and monitored by machine vision. (b) Image of the μRD manufacturing system at the University of Illinois at Urbana-Champaign. Figure is used with permission from the American Society of Mechanical Engineers.

Table 1. Fabrication Parameters.

Parameter	Value	Product Number
Syringe size	5 mL	Nordson EFD 7012094 and 7012174
Nozzle inner diameter, d	0.510 mm	Nordson EFD 7005005
Tip speed, v	3–5 mm sec^{-1}	—
Nominal extrusion rate, Q	$Q = (\pi/4)d^2v$ mm^3 sec^{-1}	—
Layer-to-layer spacing	0.420 mm	—
Filament-to-filament spacing	0.960 mm	—

can range from 200 to 500 μm (figure 2(a)), depending on the nozzle diameter. The particular μRD manufacturing system in this study has four individually addressable micro-extrusion systems, permitting up to four unique building materials and/or filament sizes to be integrated within a single scaffold [61]. The micro-extruders are indexed to operate one at a time in a sequential fashion. The entire deposition process is monitored by a computer vision system. A central control computer coordinates the actuation of each position and extrusion axis by interpreting the G-Code file described in section 2.2.

The material extrusion rate is nominally given by $Q = \frac{\pi}{4}d^2v$, where extrusion rate Q is a function of the nozzle inner diameter d and nozzle tip speed v. Manufacturing parameters are given in table 1. Tip speed ranges from 3 to 5 mm sec^{-1} depending on the complexity of the scaffold. Nozzle inner diameter and layer-to-layer and filament-to-filament spacing directly affect the dimensions Ø, H, and W in figure 1 after sintering. The scaffold designs detailed in section 2.4 require between a few dozen and a few hundred filament starts and stops, depending on size and complexity. Accurate filament starting and stopping requires an extrusion rate control method that is more sophisticated than the simple static relationship given above. We use machine vision feedback and learning-based control to automatically construct a library of calibration maps that are accessed by the central computer to perform the correct plunger displacement profile for transient flow rate modulation; details on this algorithm can be found in [45] and [68].

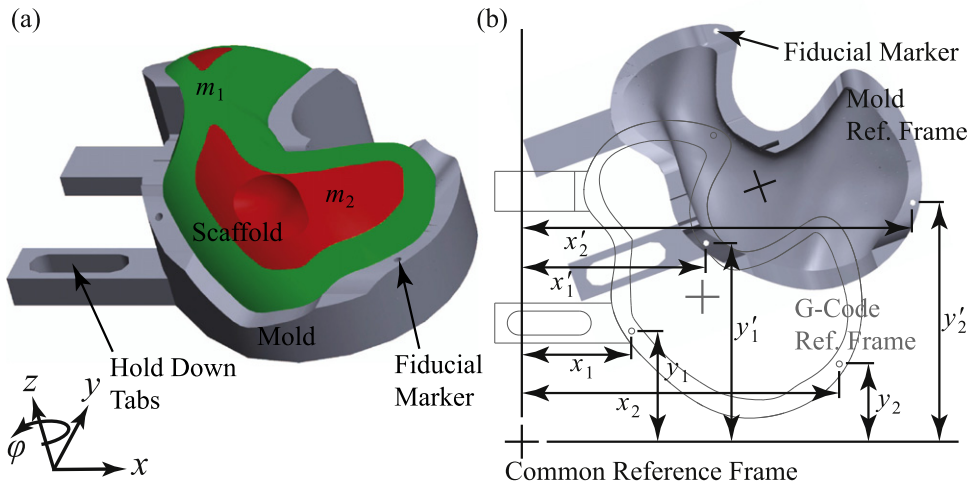

Figure 3. Scaffold manufacturing within a mold to support unsupported features. (a) Schematic of the complex Design 5 (section 2.4.3) mounted within a mold. The mold has hold-down tabs and fiducial markers for secure mounting and registration between the G-Code frame-of-reference and the mold frame-of-reference. (b) Schematic of the measurement of fiducial markers to transform G-Code coordinates.

The accurate start-stop capability enables two different filaments to abut, thereby seamlessly integrating multiple materials into a single scaffold. Lastly, the computer software automatically performs periodic nozzle cleaning operations at a cleaning station to remove accumulated building material debris and thus improve fabrication quality [61].

Given the layer-by-layer manufacturing employed by μRD and other AM technologies and the complex contoured scaffolds derived from medical imaging data, there will inevitably be large unsupported spans in the fabrication process that must be supported by a sacrificial or temporary structure. We fabricate scaffolds within a mold to support overhanging features (figure 3(a)). For every unique scaffold envelope, a new mold is designed in 3D CAD software by: (1) taking a Boolean subtraction of the desired scaffold and the mold die; (2) removing material above the complex, multiplane contour that defines the region of the overhanging features; (3) adding fiducial markers for mold alignment; (4) adding hold-down tabs; and (5) adding small (0.25 mm) capillaries to permit oil to immerse the scaffold during fabrication. Molds are fabricated as described in section 2.1. The mold is lightly sprayed with a release agent (Aqua Net, Lornamead Inc.) and then mounted on the substrate; however, it is impossible to perfectly register the mold frame of reference with the robot frame of reference in the x-y plane. To compensate for the deviation in frame of reference, we use the position sensors on the stages and the alignment of the nozzle with fiducial markers on the mold to transform the G-Code coordinates such that the part is fabricated accurately within the mold. The transformation is given by

$$\begin{bmatrix} X' \\ Y' \\ Z' \end{bmatrix} = \begin{bmatrix} \cos\varphi & \sin\varphi & 0 \\ -\sin\varphi & \cos\varphi & 0 \\ 0 & 0 & 1 \end{bmatrix} \begin{bmatrix} X - (x_1 + x_2)/2 \\ Y - (y_1 + y_2)/2 \\ Z - (z_1 + z_2)/2 \end{bmatrix} + \begin{bmatrix} (x'_1 + x'_2)/2 \\ (y'_1 + y'_2)/2 \\ (z'_1 + z'_2)/2 \end{bmatrix}, \quad (2)$$

where

$$\phi = \tan^{-1}\left(\frac{y_2 - y_1}{x_2 - x_1}\right) - \tan^{-1}\left(\frac{y'_2 - y'_1}{x'_2 - x'_1}\right),$$

x, y, and z are the coordinates of ideal fiducials that are aligned with the nominal G-Code file, x', y', and z' are the measured coordinates of fiducials on the mold, X, Y, and Z are the coordinates in a line of G-Code, and X', Y', and Z' are the transformed G-Code coordinates (figure 3(b)). Transformation (2) assumes that the substrate is parallel to the x-y plane of the gantry position system and thus out-of-plane rotations in the θ and ψ Euler angles are not necessary. Similar transformations have been used by researchers to fabricate a scaffold within a skeletal cavity [35].

Scaffolds are fabricated within an oil bath (paraffin oil, Lamplight Ultrapure) that slows the evaporation of the colloidal building material solvent, thereby ensuring that the structure dries uniformly; nonuniform evaporation drives a gradient in scaffold shrinkage and thus leads to structural stress gradients. Fabricated scaffolds are left to solidify under oil for 12 h and then left to dry in air for another 24 h. As a scaffold dries, the total dimension shrinks because of capillary-

Table 2. Sintering schedule.

Segment	Ramp Rate [°C h^{-1}]	Temperature [°C]	Hold [h]
1	180	100	1
2	60	250	4
3	60	350	0
4	180	900	2
5	600	1300	2
6	natural cooling	ambient	—

driven particle consolidation [69], which delaminates the scaffold from the surface of the mold. Dried scaffolds are carefully removed from the mold; these green body scaffolds are robust enough to be handled carefully, but require sintering to achieve full strength. Scaffolds are sintered in a furnace using a temperature profile that culminates in a temperature dwell at 1300 °C for two h (table 2) to fully densify the scaffold and fuse the HA particles [61]. At 1300 °C, HA will thermally decompose into TCP products, with previous studies using identical HA particles and sintering routines reporting a 13% β-TCP phase [48, 64]. Fully sintered scaffolds shrink to a size that is 77.7% $\pm$ 4.9% (mean $\pm$ standard deviation, sample size of 1944 measurements) of the size defined by G-Code; shrinkage is calculated by micro-Computed Tomography (μCT) measurements of representative scaffolds from our previous studies [45].

2.4. Scaffold designs

Five different scaffold designs are devised to explore the feasibility of using molds to support overhanging features in μRD. The two primary scaffold design variables are the scaffold envelope and the location of different material domains. Scaffold macroporosity is the same in all designs as the authors have explored this design space in previous works [45]. Macroporosity designs are nominally Ø = 398 μm, H = 257 μm, and W = 351 μm after sintering (figure 1). The basic behavior of the colloidal materials interfacing with a mold is explored in a set of simple cylinders with constant-slope conical cavities in design 1. Designs 2–4 explore regular canonical shapes that incorporate continually changing envelope slopes and multiple material domains. The lessons learned from designs 1–4 are integrated into a scaffold with a complex envelope defined by an orbital socket defect and multiple material domains in design 5; this design also demonstrates the translation of medical CT data into a manufactured scaffold and thus highlights a clinically applicable workflow.

2.4.1. Design 1

An array of six cylinders, each with a concave, conical cavity of a different draft angle slope (4/1, 2/1, 4/3, 1/1, 4/5, and 2/3), are used to evaluate the draft angle at which a scaffold is self-supporting and the draft angle at which the scaffold will delaminate from a mold without producing defects (figure 4). Material m_1 is used for each. As the slope of the conical cavity decreases, the deposition surface of the mold becomes more like the flat substrates typically used in μRD, and it is anticipated that the scaffold will easily delaminate from the mold during drying-induced shrinkage without defects. As the slope increases, the compressive stress normal to the mold surface will increase during shrinkage, possibly leading to cracking of the green body. However, at steep draft angle slopes, accurate deposition should be possible without support because the scaffold edges are nearly vertical, so each layer has base support from previous layers [66]. To test these scenarios, each of the six scaffolds is fabricated with and without mold support for a total of twelve scaffolds.

2.4.2. Designs 2–4

Designs 2–4 (figure 5) are three canonical scaffolds that collectively demonstrate complex scaffold envelopes with constantly changing slopes, multiple integrated domains with different microporosities, the self-supporting nature of internal structures with steep draft angles, and the ability to have concave envelope features. Each design has overhangs that must be supported with molds. Designs 2 and 3 are indistinguishable from the external architecture, but design 2 is a test of a dissimilar material interface—such dissimilar material interfaces are seen at the cortical-to-trabecular transition in natural bone—and design 3 has a large internal cavity, as is seen in marrow space in bones. The torus in design 4 has both convex and concave features. Much like design 1, with design 4 there is a concern of shrinkage-induced binding of the scaffold on the mold on the concave features; the convex features should not be an issue, as shrinkage pulls the scaffold away from the mold surface. Notably, designs 2 and 3 have a radial/concentric pattern, and design 2 integrates this pattern with a rectangular lattice. The freeform nature of μRD permits fairly arbitrary filament alignment, hence macropore structures, provided that unsupported spans do not exceed approximately 2 mm [62].

2.4.3. Design 5

Design 5 has a scaffold envelope that is derived from a hypothetical orbital socket defect (figure 1). The orbital socket is one of the most architecturally complex regions of the human skeleton and is thus a rigorous test of the manufacturability of biologically inspired, complex-contour, multi-domain scaffolds. Manufacturing success requires an integration of the scaffold manufacturing capabilities explored in designs 1–4: accurate extrusion starting and stopping, integration of different materials, and registration with and manufacturing within a mold. We use a clinically relevant data processing pipeline: the 3D scaffold envelope is derived from μCT data cataloged in the Visual Human Project; we select the skull skeletal

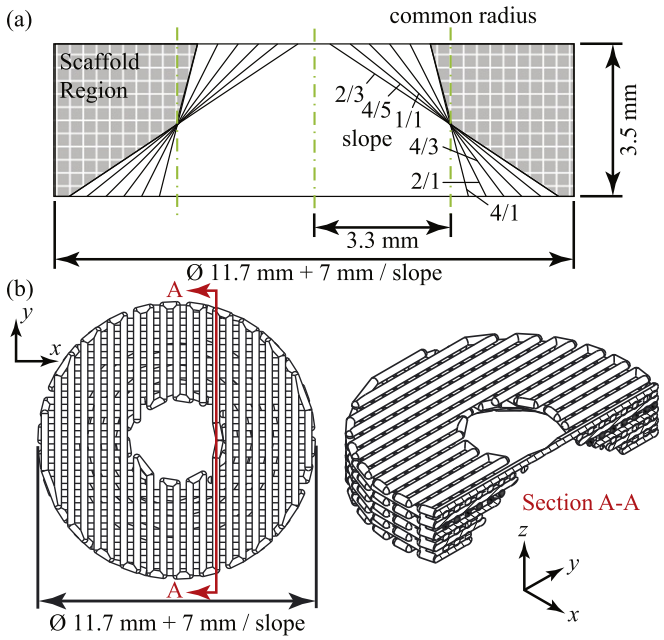

Figure 4. Set of six test scaffolds to evaluate the self-supporting nature of material filament in μRD and manufacturing with a mold. (a) Cross-section of each cylinder demonstrating the different draft angles tested. (b) 3D model of Design 1 with a draft angle of 4/5. The plan view and cross-section through the isometric view demonstrate the conical cavity.

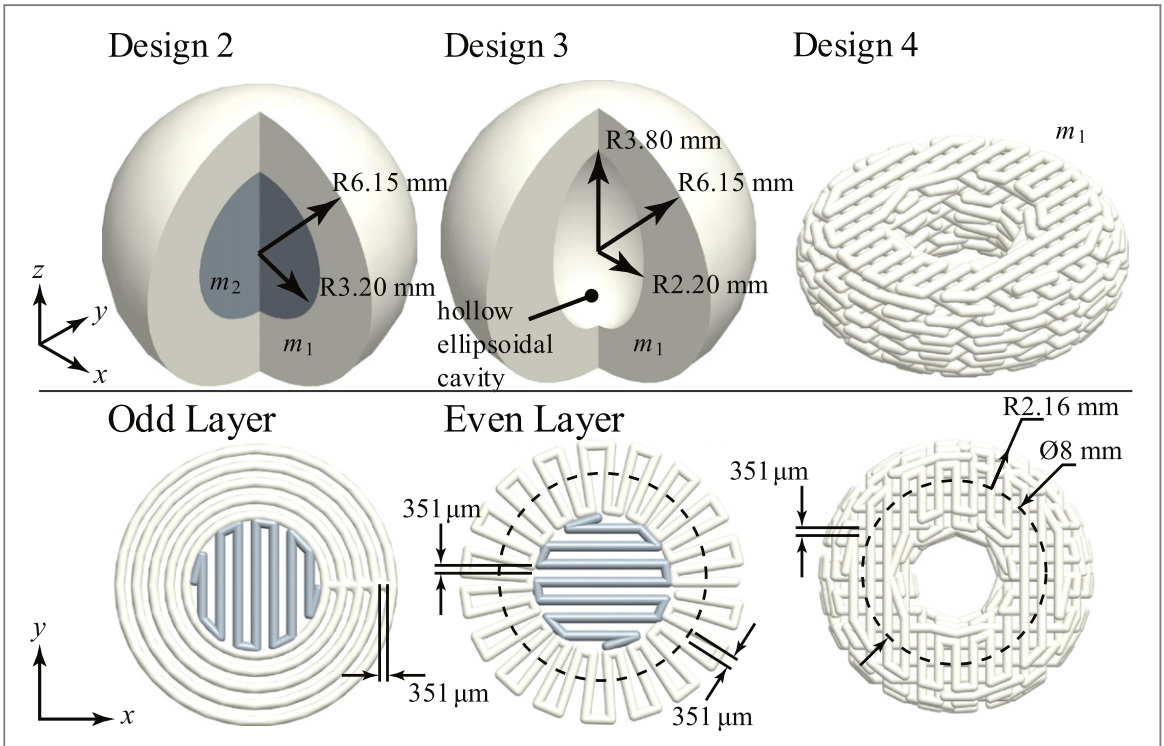

Figure 5. Designs 2–4 are canonical shapes to evaluate fabrication within a mold and the integration of multiple material domains. Figure is used with permission from the American Society of Mechanical Engineers.

structure in the Visual Human Project [70] and then digitally excise the orbital socket to serve as a model defect; the negative of the orbital socket defect is used as the scaffold envelope; the 3D region near the skeletal surface is designated as material m_1, to best mimic the mechanical properties of cortical bone; the internal region is designated as material m_2, to best mimic the mechanical properties of trabecular bone [29, 44, 48]; and then, finally, the 3D model is scaled up by 28% to account for the drying- and sintering-induced shrinkage (section 2.3). The scaffold envelope has many convex and concave contours and hence is a demonstration of whether the draft angle limitations of concave features explored in design 1 extend to larger,

more complex scaffolds. Unlike the axially symmetric scaffolds in designs 1–4, design 5 requires the proper registration of mold features with G-Code instructions in the φ angle, in addition to the typically required x, y, and z coordinate registrations.

2.5. Characterization

A suite of imaging tools is used to characterize the scaffolds. Each fabricated scaffold is imaged by macro photography (Canon EOS-5D Mark III) to characterize filaments and total scaffold structure. Multiple μCT instruments are used to characterize internal macroporosity and demonstrate differences in x-ray attenuation of the different material domains; each μCT instrument has different chamber sizes and accompanying algorithms. X-ray attenuation images are taken with a SkyScan 1172 for designs 1–4 and an Xradia MicroXCT-400 for design 5 due to the large dimension of design 5; two μCT scans are performed on different regions of design 5 and the resulting images are digitally stitched together using overlapping part recognition. A third μCT instrument (μCT 80, Scanco Medical) is used to quantify the distribution of macropore and filament sizes of designs 2–5; design 1 is only used to assess fabrication on a mold. Quantification is performed using Scanco Eval V6 software. In order to not introduce measurement artifacts from the edge of the scaffolds, contours are placed on the inner edge of the outermost filament in each slice, and hollow regions at the center of designs 3 and 4, and the regions outside the contours are removed from the analysis. Scaffolds are segmented by application of a global threshold corresponding to 360 mg HA cm^{-3} and a low-pass Gaussian filter (sigma 0.8, support 1.0) to suppress noise. Macropore and filament sizes are quantified using a built-in algorithm that fits a maximal sphere in either the macropore or filament body at each voxel in the 3D space [71]. Distributions are reported as histograms, normalized based on volume percentage (histogram bin sizes are 10 μm for designs 2–4 and 25 μm for design 5). Lastly, SEM (Philips XL30 ESEM-FEG) is used to characterize the microstructural differences between materials m_1 and m_2 in a representative scaffold.

3. Results

3.1. Designs 1a–1f

All twelve scaffolds were fabricated in an identical process, with the only differences being the G-Code file that prescribed the design and whether or not a mold was used. All scaffolds were manufactured without appreciable extrusion-related defects and thus the mold versus no-mold comparison is fair. Scaffolds fabricated with a mold to support overhanging features (figure 6(a)) maintained the conical cavities for all slopes. Scaffolds fabricated without a mold could only maintain a conical cavity for draft angle slopes of 2/1 and larger (figure 6(g)). Scaffolds with a shallow draft angle were not self-supporting and the center of the cylinder collapsed (figure 6(d)), and therefore the geometric integrity of the scaffold was compromised. The advantage of fabricating scaffolds with overhanging features was best demonstrated with μCT images of the internal macroporous architecture; scaffolds deposited on a mold maintained a uniform filament and macropore structure (figure 6(e)) while scaffolds deposited without a mold collapsed and therefore deformed the macropore structure (figure 6(f)). There were no observed negative consequences of using a mold to support overhanging features for this simple design: all scaffolds successfully released from the mold surface, and the precise mold registration procedure ensured that the nozzle navigated around the mold surface without collisions or excessive deformation of the extruded filaments at the mold surface (figure 6(c)).

3.2. Designs 2–4

Similar to design 1, there was no evidence of sintering- or shrinking-induced cracking, either from the interface between two different material domains, in design 2, or from constrained shrinking around the mold supporting the concavity in design 4 (figure 7). On the surface, designs 2 and 3 looked identical, but the difference between the designs was clear from the reconstructed μCT data in column 3. The ellipsoidal cavity in design 3 maintained its shape despite being unsupported; the cavity had a steep slope throughout most of the layer-by-layer build routine and therefore was self-supporting. At the top of the ellipsoid, the slope rapidly becomes shallower, but at this location the distance to be spanned by a filament was short and an ellipsoidal cavity could be completed with little deviation from the desired design. Logically, not all hollow cavities would be self-supporting, but some cavity designs could be, and thus demonstrated promise for recreating anatomically derived marrow cavities. Measured architectural features of macropore size and filament thickness approximated the nominal dimensions designed in section 2.4 (see table 3 and figure 8); all peak bin frequencies and means for the macropore and filament sizes were within 100 μm of the nominal and, based on animal model studies [42, 43], we predict that the *in vivo* response would be insensitive to manufacturing variations of this magnitude.

3.3. Design 5

Design 5 was considerably larger than each of designs 1–4 and thus took longer than 10 h to fabricate in the mold. After fabrication, the scaffold was allowed 36 h to dry, after which we were able to release the scaffold from the mold with no observable cracking or defects, as determined by macrophotography and μCT

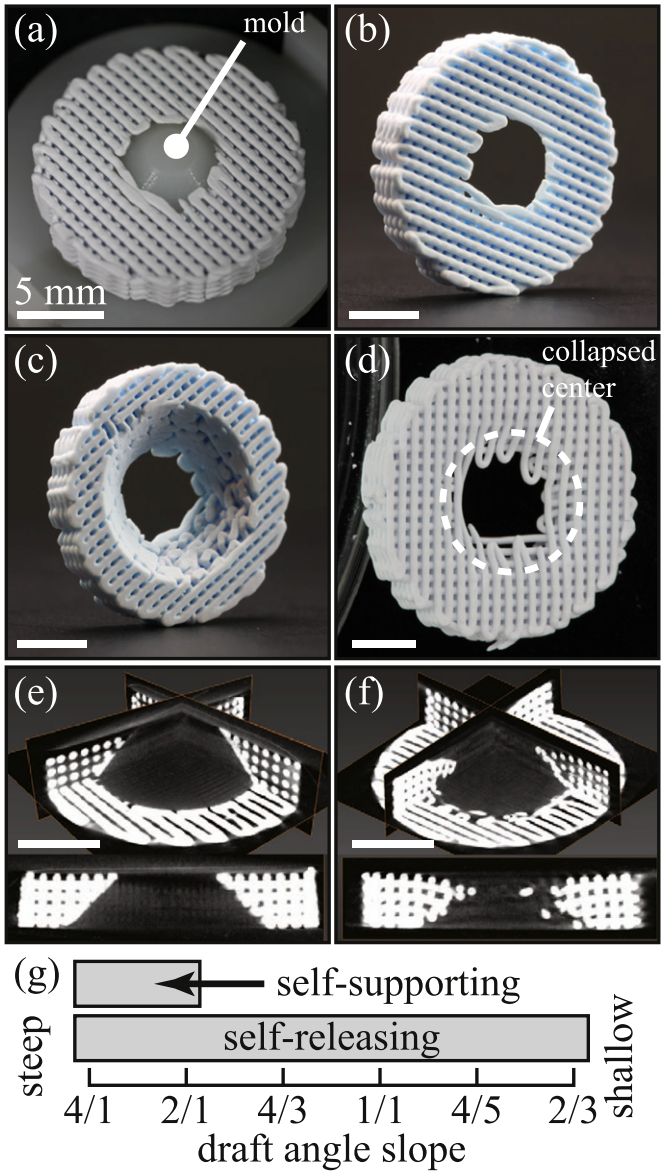

Figure 6. Manufacturing results for design 1. (a)–(c) Representative scaffold with a 4/5 draft angle slope fabricated on top of a mold to support the conical cavity. (a) As-fabricated scaffold on the mold. (b) and (c) As-sintered scaffold from the top and bottom directions, respectively. (d) Representative scaffold with a designed 4/5 draft angle slope fabricated without a mold. The overhanging features collapsed during fabrication. (e) μCT image of a representative scaffold with a 4/5 draft angle slope demonstrating that a supporting mold helped maintain the internal macroporous architecture. (f) μCT image of a representative scaffold with a 4/5 draft angle slope fabricated without a support mold. A 4/5 draft slope was not self-supporting and thus the overhanging region collapsed. (g) Synopsis of manufacturing results. All scaffolds released from the mold surface. Scaffolds with a draft angle slope of greater than 2/1 were self-supporting and did not need mold support.

imaging. Notably, design 5 has a large concave contour that corresponded to the orbital socket side of the scaffold that we anticipated would cause some difficulty as the scaffold dried and thus shrank around the mold; however, this contour did not cause cracking from constrained shrinkage. The two different material domains, materials m_1 and m_2, were fully fused together with no observable delamination at their interfaces (figure 9). A representative scanning electron micrograph from a smaller, simpler scaffold demonstrated that the interface between the two materials was continuous without delamination (figure 1). Pockets between the two different domains, where they existed, existed because of deposition inaccuracies, not material delamination. Although the filaments were largely uniform in size and spacing across the entire scaffold, design 5 did have a higher frequency of manufacturing defects, as evidenced by the right-sided tail in macropore and filament size distributions (figure 8). As reported elsewhere, large build sizes do complicate μRD fabrication as small defects compound layer-by-layer, causing a positive feedback loop of fabrication errors [63]; a defect in the previous layer can affect filament adhesion in the current layer, which then negatively affects the subsequent layer. Again, peak macropore and filament dimensions were within 110 μm of the nominal dimensions (table 3) and thus were in a range in which

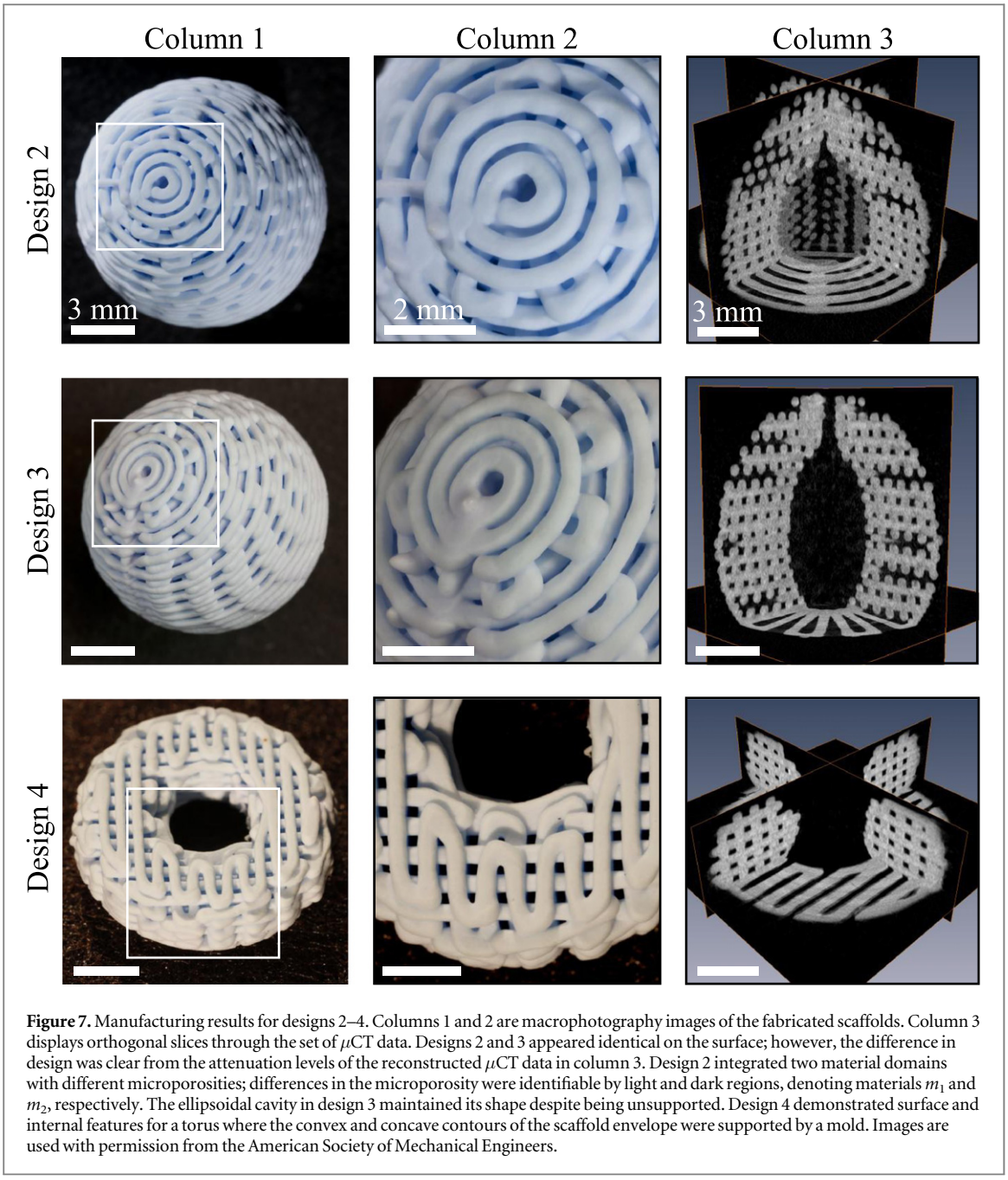

Figure 7. Manufacturing results for designs 2–4. Columns 1 and 2 are macrophotography images of the fabricated scaffolds. Column 3 displays orthogonal slices through the set of μCT data. Designs 2 and 3 appeared identical on the surface; however, the difference in design was clear from the attenuation levels of the reconstructed μCT data in column 3. Design 2 integrated two material domains with different microporosities; differences in the microporosity were identifiable by light and dark regions, denoting materials m_1 and m_2, respectively. The ellipsoidal cavity in design 3 maintained its shape despite being unsupported. Design 4 demonstrated surface and internal features for a torus where the convex and concave contours of the scaffold envelope were supported by a mold. Images are used with permission from the American Society of Mechanical Engineers.

Table 3. Quantified fabrication accuracy metrics. Means and standard deviations are rounded to reflect bin sizes.

Metric	Design	Peak Bin Frequency [μm]	Mean [μm]	Standard Deviation [μm]
Macropore Size	2	210	240	120
	3	210	240	90
	4	290	250	70
	5	325	350	225
Filament Size	2	490	470	180
	3	430	430	100
	4	480	460	90
	5	425	500	150

the *in vivo* response would be insensitive to manufacturing variation. The overall manufacturing quality demonstrates that large scaffolds, larger in total dimension than critical size, with advanced architecture features, can be accurately fabricated.

4. Discussion

4.1. This manufacturing paradigm enables the next generation of CaP scaffold design architectures

This work demonstrates that scaffolds composed of CaP materials can now have advanced architectural designs. This enables capabilities including complex

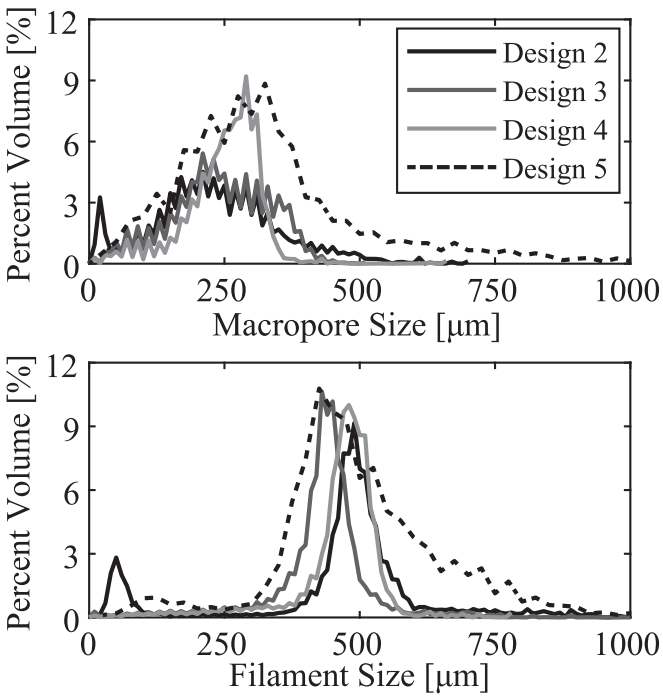

Figure 8. Fabricated macropore and filament pore dimensions for designs 2–5. Percent volumes of each macropore and filament size are calculated via a maximal sphere fitting algorithm applied at all voxels in the reconstructed μCT data (section 2.5). Histogram peaks are approximately the same; however, design 5 has a larger right-sided tail in both macropore and filament sizes, indicating less accurate filament placement.

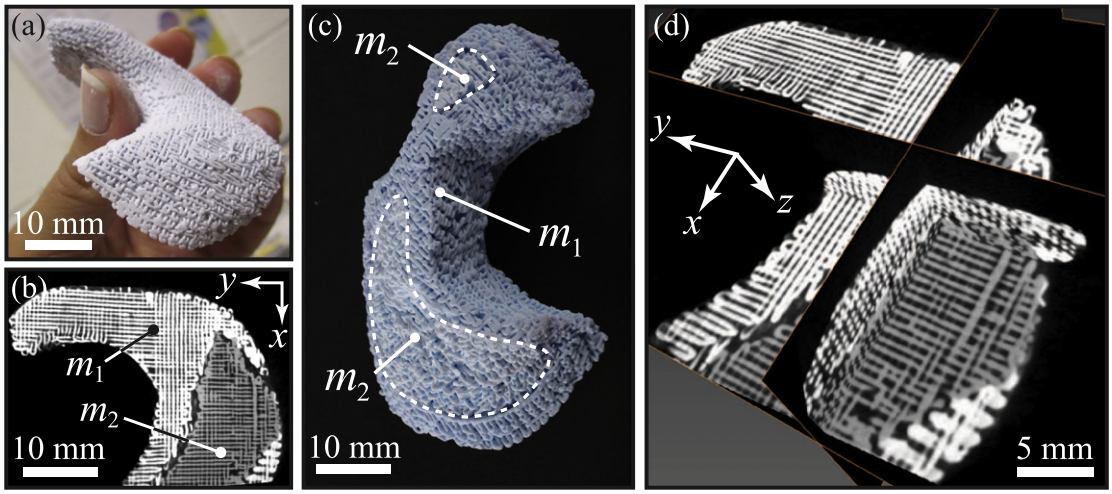

Figure 9. Design 5 fabrication results. (a) The fabricated scaffold delaminated from the mold surface when drying and thus demonstrated that even scaffolds that have a more complex envelope than those studied in designs 1–4 can be successfully fabricated within a mold. (b) Cross-section image through the *x*-*y* plane of the μCT data set. Materials m_1 and m_2 had different x-ray attenuation levels, denoted by the difference in grayscale values. (c) Optical photograph of the sintered scaffold. The multiple material domains were visible as a slight color mismatch of the different materials; a superimposed region denotes the boundary. (d) Three orthogonal cross-sections in the μCT data set. Qualitatively, the filament spacing in the *x*—*y*, *x*—*z*, and *y*—*z* planes is largely uniform.

contours in the scaffold envelope, large unsupported cavities in some designs, and multiple integrated CaP material domains. In this study we investigated the integration of different domains of HA with different microstructures: a fully dense material, m_1, and a nominally 50 vol% microporous material, m_2. However, the material set demonstrated for μRD includes β-tricalcium phosphate (β-TCP) [72, 73] and HA:TCP and HA:β-TCP composites of varying ratios [73, 74]. Each of these material chemistries can integrate pore-forming PMMA microbeads, as detailed in section 2.1, such that chemistry and microporosity can be independently controlled. Our recent studies of the *in vivo* response of HA with high volumes of microporosity found that capillary forces from the microporous structure drive osteoprogenitor cells and proteins deep

within scaffold material and improve bone growth uniformity [53–55]. Given that each of the CaP materials have different mechanical properties and bioactivity and that microporosity increases bioactivity but mechanically weakens the scaffold, the manufacturing paradigm presented here provides the scaffold designer with a powerful toolset to tailor local scaffold mechanics and bioactivity.

We envision tailored scaffold architectures that have both the requisite strength and favorable *in vivo* response designed using interlaid regions of dense, strong HA filaments and highly bioactive high-microporosity HA or HA:TCP composites. We reiterate that the manufacturing capabilities demonstrated here are all readily attainable for polymeric and polymer/ceramic composite scaffolds fabricated by modern AM tools. These advanced architectures have not previously been fabricable with CaP materials; this manufacturing development is a step in the direction of this next generation of CaP scaffold designs.

4.2. Our manufacturing paradigm appreciably expands the set of feasible scaffold envelopes

The results in this manuscript demonstrate that many of the features that are included in advanced architecture bone scaffolds, including convex and concave features, multiple material domains, and internal concavities, are feasible using the described manufacturing paradigm. Importantly, our μRD system and accompanying control algorithms use:

- a materials set in which each material has a carefully tuned rheology such that it is self-supporting at steep draft angles and has a matched rheology so that abutting materials do not grossly deform each other,
- molds to support features that are not self-supporting, as illuminated by the study of design 1, and
- a robust control system to carefully control filament placement.

Although these capabilities permit a vast array of complex scaffolds to be fabricated, some scaffold designs are infeasible. One such design has unsupported features in which the requisite support mold would block the fabrication of underlying features using the top-down, layer-by-layer paradigm employed by μRD. These limitations have implications for clinically applicable scaffold designs as well. The orbital socket scaffold in design 5 would require through holes for screw fixation; either the cylindrical cavity that defines these through holes would have to be oriented approximately perpendicular to the μRD system x-y plane or previously described postprocess machining [5, 44, 53, 54] would have to be employed.

4.3. The utilization of molds is efficient and permits clinical translation

Arguably, an ideal scaffold manufacturing tool would not require molds for unsupported features and would simply use sacrificial support materials. Section 1 argues why sacrificial materials, which are most likely polymeric, are not easily integrable for CaP scaffold manufacture. Prefabricated molds present a simple, inexpensive solution that enables scaffold envelopes with complex contours. Importantly, given a digital 3D description of the scaffold envelope, these molds can be designed and fabricated in hours and thus do not delay the clinically important workflow of defect imaging, scaffold design, scaffold manufacturing, seeding with biologics, and then implantation [5, 13, 75].

5. Conclusions

This manuscript details a demonstration of manufacturing capabilities of a multimaterial direct-write additive manufacturing tool, micro-Robotic Deposition (μRD), used in conjunction with a mold, and accompanying coordinate transformations, to fabricate calcium phosphate (CaP) scaffolds with complex 3D envelopes and multiple material domains. These capabilities are readily available with polymer and polymer/CaP composites with commercial additive manufacturing tools, but have not been demonstrated with fully dense and pure CaP materials. The ultimate demonstration is a CaP scaffold with an envelope that is defined by medical imaging data and user-defined regions of different CaP microstructures. These capabilities highlight a path towards highly tailorable 3D scaffold designs. Previously established materials formulations have provided raw building materials that span the set of efficacious CaP materials and have a range of microstructures (0–60 vol% interconnected microporosity and 1–10 μm pore interconnection size [48, 60]). With the established multimaterial capabilities of μRD and with our control methods and ability to fabricate complex envelopes, defect-specific scaffolds with locally customizable material domains are now feasible. These tools expand the set of scaffold designs fabricable with CaP materials; in particular, we envision mechanically and bio-actively optimized scaffolds that integrate dense HA load-bearing members with highly efficacious microporous HA or TCP.

Acknowledgments

The authors gratefully acknowledge the National Library of Medicine of the United States for access to the data in the Visual Human Project that was used in design 5, Samantha Polak for her assistance with Visual Human Project data manipulation, Shelby Svientek for her assistance with macrophotography imaging, and Leilei Yin and the Imaging Technology Group at the Beckman Institute at the University of

Illinois at Urbana-Champaign for the use of their facilities and assistance with μCT instrumentation and image processing. This work was supported in part by NSF Award 09-00184 ARRA, University of Notre Dame capitalization funds, and University of Illinois at Urbana-Champaign internal funds.

References

[1] Spicer P P, Kretlow J D, Young S, Jansen J A, Kasper F K and Mikos A G 2012 Evaluation of bone regeneration using the rat critical size calvarial defect *Nat. Protocols* **7** 1918–29
[2] Cooper G M, Mooney M P, Gosain A K, Campbell P G, Losee J E and Huard J 2010 Testing the critical size in calvarial bone defects: revisiting the concept of a critical-size defect *Plast. Reconstr. Surg.* **125** 1685–92
[3] Porter J R, Ruckh T T and Popat K C 2009 Bone tissue engineering: a review in bone biomimetics and drug delivery strategies *Biotechnol. Prog.* **25** 1539–60
[4] Kolambkar Y M, Boerckel J D, Dupont K M, Bajin M, Huebsch N, Mooney D J, Hutmacher D W and Guldberg R E 2011 Spatiotemporal delivery of bone morphogenetic protein enhances functional repair of segmental bone defects *Bone* **49** 485–92
[5] Cesarano J, Dellinger J G, Saavedra M P, Gill D D, Jamison R D, Grosser B A, Sinn-Hanlon J M and Goldwasser M S 2005 Customization of load-bearing hydroxyapatite lattice scaffolds *Int. J. Appl. Ceram. Technol.* **2** 212–20
[6] Giannoudis P V, Einhorn T A and Marsh D 2007 Fracture healing: the diamond concept *Injury* **38** (Suppl 4) S3–6
[7] Giannoudis P V, Faour O, Goff T, Kanakaris N and Dimitriou R 2011 Masquelet technique for the treatment of bone defects: tips-tricks and future directions *Injury* **42** 591–8
[8] Roberts S J, van Gastel N, Carmeliet G and Luyten F P 2015 Uncovering the periosteum for skeletal regeneration: the stem cell that lies beneath *Bone* **70** 10–8
[9] Cattaneo R, Catagni M A and Guerreschi F 1993 Applications of the Ilizarov method in the humerus. Lengthenings and nonunions *Hand Clin.* **9** 729–39
[10] Silber J S, Anderson D G, Daffner S D, Brislin B T, Leland J M, Hilibrand A S, Vaccaro A R and Albert T I 2003 Donor site morbidity after anterior iliac crest bone harvest for single-level anterior cervical discectomy and fusion *Spine* **28** 134–9
[11] Atala A, Bauer S B, Soker S, Yoo J J and Retik A B 2006 Tissue-engineered autologous bladders for patients needing cystoplasty *The Lancet* **367** 1241–6
[12] Atala A, Kasper F K and Mikos A G 2012 Engineering complex tissues *Sci. Transl. Med.* **4** 160rv12
[13] Hollister S J and Murphy W L 2011 Scaffold translation: barriers between concept and clinic *Tissue Eng.* B **17** 459–74
[14] Hollister S J 2009 Scaffold design and manufacturing: from concept to clinic *Adv. Mater.* **21** 3330–42
[15] Hing K A, Best S M, Tanner K E, Bonfield W and Revell P A 2004 Mediation of bone ingrowth in porous hydroxyapatite bone graft substitutes *J. Biomed. Mater. Res.* **68A** 187–200
[16] Hing K A, Annaz B, Saeed S, Revell P A and Buckland T 2005 Microporosity enhances bioactivity of synthetic bone graft substitutes *J. Mater. Sci. Mater. Med.* **16** 467–75
[17] Lin C Y, Kikuchi N and Hollister S J 2004 A novel method for biomaterial scaffold internal architecture design to match bone elastic properties with desired porosity *J. Biomech.* **37** 623–36
[18] Xiong Z 2002 Fabrication of porous scaffolds for bone tissue engineering via low-temperature deposition *Scr. Mater.* **46** 771–6
[19] Kalita S J, Bose S, Hosick H L and Bandyopadhyay A 2003 Development of controlled porosity polymer-ceramic composite scaffolds via fused deposition modeling *Mater. Sci. Eng.* C **23** 611–20
[20] Liu L, Xiong Z, Yan Y, Zhang R, Wang X and Jin L 2009 Multinozzle low-temperature deposition system for construction of gradient tissue engineering scaffolds *J. Biomed. Mater. Res.* B *Appl. Biomater.* **88B** 254–63
[21] Domingos M, Intranuovo F, Russo T, Santis R D, Gloria A, Ambrosio L, Ciurana J and Bartolo P 2013 The first systematic analysis of 3D rapid prototyped poly(ε-caprolactone) scaffolds manufactured through BioCell printing: the effect of pore size and geometry on compressive mechanical behaviour and *in vitro* hMSC viability *Biofabrication* **5** 045004
[22] Kim G, Ahn S, Yoon H, Kim Y and Chun W 2009 A cryogenic direct-plotting system for fabrication of 3D collagen scaffolds for tissue engineering *J. Mater. Chem.* **19** 8817
[23] Hutmacher D W, Schantz J T, Lam C X F, Tan K C and Lim T C 2007 State of the art and future directions of scaffold-based bone engineering from a biomaterials perspective *J. Tissue Eng. Regen. Med.* **1** 245–60
[24] Visser J, Melchels F P W, Jeon J E, van Bussel E M, Kimpton L S, Byrne H M, Dhert W J A, Dalton P D, Hutmacher D W and Malda J 2015 Reinforcement of hydrogels using three-dimensionally printed microfibres *Nat. Commun.* **6** 6933
[25] Inzana J A, Olvera D, Fuller S M, Kelly J P, Graeve O A, Schwarz E M, Kates S L and Awad H A 2014 3D printing of composite calcium phosphate and collagen scaffolds for bone regeneration *Biomaterials* **35** 4026–34
[26] Khalyfa A, Vogt S, Weisser J, Grimm G, Rechtenbach A, Meyer W and Schnabelrauch M 2007 Development of a new calcium phosphate powder-binder system for the 3D printing of patient specific implants *J. Mater. Sci. Mater. Med.* **18** 909–16
[27] Castilho M, Dias M, Gbureck U, Groll J, Fernandes P, Pires I, Gouveia B, Rodrigues J and Vorndran E 2013 Fabrication of computationally designed scaffolds by low temperature 3D printing *Biofabrication* **5** 035012
[28] Castilho M, Rodrigues J, Pires I, Gouveia B, Pereira M, Moseke C, Groll J, Ewald A and Vorndran E 2015 Fabrication of individual alginate-TCP scaffolds for bone tissue engineering by means of powder printing *Biofabrication* **7** 015004
[29] Wagoner Johnson A J and Herschler B A 2011 A review of the mechanical behavior of CaP and CaP/polymer composites for applications in bone replacement and repair *Acta Biomater.* **7** 16–30
[30] Bertassoni L E *et al* 2014 Direct-write bioprinting of cell-laden methacrylated gelatin hydrogels *Biofabrication* **6** 024105
[31] Hockaday L A *et al* 2012 Rapid 3D printing of anatomically accurate and mechanically heterogeneous aortic valve hydrogel scaffolds *Biofabrication* **4** 035005
[32] Khoda A K M B, Ozbolat I T and Koc B 2011 Engineered tissue scaffolds with variational porous archictecture *J. Biomech. Eng.* **133** 011001–1
[33] Barry R A, Shepherd R F, Hanson J N, Nuzzo R G, Wiltzius P and Lewis J A 2009 Direct-write assembly of 3D hydrogel scaffolds for guided cell growth *Adv. Mater.* **21** 2407–10
[34] Cohen D L, Malone E, Lipson H and Bonassar L J 2006 Direct freeform fabrication of seeded hydrogels in arbitrary geometries *Tissue Eng.* **12** 1325–35
[35] Cohen D L, Lipton J I, Bonassar L J and Lipson H 2010 Additive manufacturing for *in situ* repair of osteochondral defects *Biofabrication* **2** 035004
[36] Sonnet C *et al* 2013 Rapid healing of femoral defects in rats with low dose sustained BMP2 expression from PEGDA hydrogel microspheres *J. Orthop. Res.* **31** 1597–604
[37] Mahadik B P, Pedron Haba S, Skertich L J and Harley B A C 2015 The use of covalently immobilized stem cell factor to selectively affect hematopoietic stem cell activity within a gelatin hydrogel *Biomaterials* **67** 297–307
[38] Banks J M, Mozdzen L C, Harley B A C and Bailey R C 2014 The combined effects of matrix stiffness and growth factor immobilization on the bioactivity and differentiation capabilities of adipose-derived stem cells *Biomaterials* **35** 8951–9

[39] Boerckel J D, Kolambkar Y M, Dupont K M, Uhrig B A, Phelps E A, Stevens H Y, García A J and Guldberg R E 2011 Effects of protein dose and delivery system on BMP-mediated bone regeneration *Biomaterials* **32** 5241–51
[40] Ahn S, Koh Y H and Kim G 2010 A three-dimensional hierarchical collagen scaffold fabricated by a combined solid freeform fabrication (SFF) and electrospinning process to enhance mesenchymal stem cell (MSC) proliferation *J. Micromech. Microeng.* **20** 065015
[41] Kane R J and Roeder R K 2012 Effects of hydroxyapatite reinforcement on the architecture and mechanical properties of freeze-dried collagen scaffolds *J. Mech. Behav. Biomed. Mater.* **7** 41–9
[42] Hing K A 2005 Bioceramic bone graft substitutes: influence of porosity and chemistry *Int. J. Appl. Ceram. Technol.* **2** 184–99
[43] Karageorgiou V and Kaplan D 2005 Porosity of 3D biomaterial scaffolds and osteogenesis *Biomaterials* **26** 5474–91
[44] Woodard J R *et al* 2007 The mechanical properties and osteoconductivity of hydroxyapatite bone scaffolds with multi-scale porosity *Biomaterials* **28** 45–54
[45] Hoelzle D J, Svientek S R, Alleyne A G and Wagoner Johnson A J 2011 Design and manufacture of combinatorial calcium phosphate bone scaffolds *J. Biomech. Eng.* **133** 101001
[46] Ricci J L, Clark E A, Murriky A and Smay J E 2012 Three-dimensional printing of bone fepair and feplacement materials: impact on craniofacial surgery *J. Craniofac. Surg.* **23** 304–8
[47] Simon J L, Michna S, Lewis J A, Rekow E D, Thompson V P, Smay J E, Yampolsky A, Parsons J R and Ricci J L 2007 *In vivo* bone response to 3D periodic hydroxyapatite scaffolds assembled by direct ink writing *J. Biomed. Mater. Res.* A **83** 747–58
[48] Cordell J M, Vogl M L and Wagoner Johnson A J 2009 The influence of micropore size on the mechanical properties of bulk hydroxyapatite and hydroxyapatite scaffolds *J. Mech. Behav. Biomed. Mater.* **2** 560–70
[49] Annaz B, Hing K A, Kayser M, Buckland T and Di Silvio L 2004 Porosity variation in hydroxyapatite and osteoblast morphology: a scanning electron microscopy study *J. Microsc.* **215** 100–10
[50] Bignon A, Chouteau J, Chevalier J, Fantozzi G, Carret J-P, Chavassieux P, Boivin G, Melin M and Hartmann D 2003 Effect of micro- and macroporosity of bone substitutes on their mechanical properties and cellular response *J. Mater. Sci. Mater. Med.* **14** 1089–97
[51] Yang Z J, Yuan H, Zou P, Tong W, Qu S and Zhang X D 1997 Osteogenic responses to extraskeletally implanted synthetic porous calcium phosphate ceramics: an early stage histomorphological study in dogs *J. Mater. Sci. Mater. Med.* **8** 697–701
[52] Yuan H, Kurashina K, de Bruijn J D, Li Y, de Groot K and Zhang X 1999 A preliminary study on osteoinduction of two kinds of calcium phosphate ceramics *Biomaterials* **20** 1799–806
[53] Lan Levengood S K, Polak S J, Wheeler M B, Maki A J, Clark S G, Jamison R D and Wagoner Johnson A J 2010 Multiscale osteointegration as a new paradigm for the design of calcium phosphate scaffolds for bone fegeneration *Biomaterials* **31** 3552–63
[54] Lan Levengood S K, Polak S J, Poellmann M J, Hoelzle D J, Maki A J, Clark S G, Wheeler M B and Wagoner Johnson A J 2010 The effect of BMP-2 on micro- and macroscale osteointegration of biphasic calcium phosphate scaffolds with multiscale porosity *Acta Biomater.* **6** 3283–91
[55] Polak S J, Rustom L E, Genin G M, Talcott M and Wagoner Johnson A J 2013 A mechanism for effective cell-seeding in rigid, microporous substrates *Acta Biomater.* **9** 7977–86
[56] Gibson I, Rosen D W and Stucker B 2010 *Additive Manufacturing Technologies: Rapid Prototyping to Direct Digital Manufacturing* (New York: Springer)
[57] Lewis J A, Smay J E, Stuecker J and Cesarano J 2006 Direct ink writing of three-dimensional ceramic structures *J. Am. Ceram. Soc.* **89** 3599–609
[58] Chhabra R P and Richardson J F 1999 *Non-Newtonian Flow and Applied Rheology: Engineering Applications* (Oxford: Butterworth-Heinemann)
[59] Lewis J A 2000 Colloidal processing of ceramics *J. Am. Ceram. Soc.* **83** 2341–59
[60] Michna S, Wu W and Lewis J A 2005 Concentrated hydroxyapatite inks for direct-write assembly of 3D periodic scaffolds *Biomaterials* **26** 5632–9
[61] Hoelzle D J 2011 Flexible adaptation of iterative learning control with applications to synthetic bone graft manufacturing *Doctoral Thesis* University of Illinois at Urbana-Champaign
[62] Smay J E, Cesarano J III and Lewis J A 2002 Colloidal inks for directed assembly of 3D periodic structures *Langmuir* **18** 5429–37
[63] Hoelzle D J, Alleyne A G and Wagoner Johnson A J 2008 Micro robotic deposition guidelines by a design of experiments approach to maximize fabrication reliability for the bone scaffold application *Acta Biomater.* **4** 897–912
[64] Cordell J M 2006 The influence of micropore size on the mechanical properties of bulk hydroxyapatite and hydroxyapatite scaffolds *Masters Thesis* University of Illinois at Urbana-Champaign
[65] Pollack H W 1990 *Computer Numerical Control* (Englewood Cliffs, NJ: Prentice-Hall)
[66] Cesarano J III, Segalman R and Calvert P 1998 Robocasting provides moldless fabrication from slurry deposition *Ceram. Ind.* **148** 94–102
[67] Lewis J A 2006 Direct writing of 3D functional materials *Adv. Funct. Mater.* **16** 2193–204
[68] Hoelzle D J, Alleyne A G and Wagoner Johnson A J 2011 Basis task approach to iterative learning control with applications to micro-robotic deposition *IEEE Trans. Control Syst. Technol.* **19** 1138–48
[69] Reed J S 1988 *Introduction to the Principles of Ceramic Processing* (New York: Wiley)
[70] US National Library of Medicine *The Visual Human Project* (http://www.nlm.nih.gov/research/visible_human.html)
[71] Hildebrand T and Ruegsegger P 1997 A new method for the model-independent assessment of thickness in three-dimensional images *J. Microsc.* **185** 67–75
[72] Miranda P, Saiz E, Gryn K and Tomsia A P 2006 Sintering and robocasting of β-tricalcium phosphate scaffolds for orthopaedic applications *Acta Biomater.* **2** 457–66
[73] Franco J, Hunger P, Launey M E, Tomsia A P and Saiz E 2010 Direct write assembly of calcium phosphate scaffolds using a water-based hydrogel *Acta Biomater.* **6** 218–28
[74] Allori A C, Lin C D, Sailon A M, Clark E, Cretiu-Vasiliu C, Smay J E, Ricci J L and Warren S M 2008 Endogenous bone engineering using solid scaffolds with time-released porosity *J. Am. Coll. Surg.* **207** S51
[75] Hollister S J 2005 Porous scaffold design for tissue engineering *Nat. Mater.* **4** 518–90